X-SEA-F-SPIDER characterization of over octave spanning pulses in the infrared range

G. Fan, T. Balčiūnas, C. Fourcade-Dutin, Stefan Haessler, A. Voronin, A. Zheltikov, Frédéric Gérôme, F. Benabid, A. Baltuška, T. Witting

X-SEA-F-SPIDER characterization of over octave spanning pulses in the infrared range

G. Fan,[1] T. Balčiūnas,[1] C. Fourcade-Dutin,[2] S. Haessler,[1,3] A. A. Voronin,[4] A. M. Zheltikov,[4,5] F. Gérôme,[2] F. Benabid,[2] A. Baltuška,[1] and T. Witting[6]

[1]*Photonics Institute Vienna University of Technology, Gusshausstrasse 27-387, A-1040 Vienna, Austria*

[2]*GPPMM group, Xlim Research Institute, UMR 7252 CNRS, University de Limoges, Limoges, France*

[3]*Laboratoire d'Optique Appliquée, ENSTA ParisTech, CNRS, Ecole polytechnique, Université Paris-Saclay, 828 bd des Maréchaux, 91762 Palaiseau cedex France*

[4]*Physics Department, International Laser Center, M.V. Lomonosov Moscow State University, 119992 Moscow, Russia*

[5]*Department of Physics and Astronomy, Texas A & M University, College Station Texas 77843-4242, USA*

[6]*Blackett Laboratory, Imperial College London, London SW7 2BW, UK*

[*]*guangyu.fan@tuwien.ac.at*

Abstract: We show a practical implementation of a pulse characterization method for sub-cycle pulse measurements in the infrared spectral range based on spectral shearing interferometry. We employ spatially-encoded arrangement filter-based spectral phase interferometry for direct electric field reconstruction with external ancila pulses (X-SEA-F-SPIDER). We show merits and limitations of the setup and an in-depth comparison to another widely used temporal characterization technique - Second-Harmonic Generation Frequency Resolved Optical Gating (SHG-FROG). The X-SEA-F-SPIDER implementation presented in this paper allows measurement of sub-cycle pulses with over one octave wide spectrum spanning the 900-2400 nm range without adding any extra dispersion due to the pulse characterization apparatus.

OCIS codes: (320.0320) Ultrafast optics; (320.7100) Ultrafast measurements; (320.7160) Ultrafast technology.

References

1. E. Goulielmakis, M. Schultze, M. Hofstetter, V. S. Yakovlev, J. Gagnon, M. Uiberacker, A. L. Aquila, E. M. Gullikson, D. T. Attwood, R. Kienberger, F. Krausz, and U. Kleineberg, "Single-Cycle Nonlinear Optics," Science **320**, 1614–1617 (2008).
2. S.-W. Huang, G. Cirmi, J. Moses, K.-H. Hong, S. Bhardwaj, J. R. Birge, L.-J. Chen, E. Li, B. J. Eggleton, G. Cerullo, and F. X. Kärtner, "High-energy pulse synthesis with sub-cycle waveform control for strong-field physics," Nat. Photonics **5**, 475–479 (2011).
3. A. Wirth, Th, I. Grguraš, J. Gagnon, A. Moulet, T. T. Luu, S. Pabst, R. Santra, Z. A. Alahmed, A. M. Azzeer, V. S. Yakovlev, V. Pervak, F. Krausz, and E. Goulielmakis, "Synthesized Light Transients," Science **334**, 195–200 (2011).
4. J. Baxter, "Spectroscopy: Probing the mid-infrared," Nat. Photonics **6**, 412–412 (2012).
5. T. Popmintchev, M.-C. Chen, A. Bahabad, M. Gerrity, P. Sidorenko, O. Cohen, I. P. Christov, M. M. Murnane, and H. C. Kapteyn, "Phase matching of high harmonic generation in the soft and hard X-ray regions of the spectrum," Proc. Natl. Acad. Sci. U.S.A. **106**, 10516–10521 (2009).

#261180 Received 15 Mar 2016; revised 25 Apr 2016; accepted 25 Apr 2016; published 1 Jun 2016

6. P. Colosimo, G. Doumy, C. I. Blaga, J. Wheeler, C. Hauri, F. Catoire, J. Tate, R. Chirla, A. M. March, G. G. Paulus, H. G. Muller, P. Agostini, and L. F. DiMauro, "Scaling strong-field interactions towards the classical limit," Nat. Physics **4**, 386–389 (2008).
7. T. Balčiūnas, C. Fourcade-Dutin, G. Fan, T. Witting, A. Voronin, A. Zheltikov, F. Gerome, G. Paulus, A. Baltuška, and F. Benabid, "A strong-field driver in the single-cycle regime based on self-compression in a kagome fibre," Nat. Communications **6**, 6117 (2015).
8. K. F. Mak, J. C. Travers, N. Y. Joly, A. Abdolvand, and P. S. J. Russell, "Two techniques for temporal pulse compression in gas-filled hollow-core kagomé photonic crystal fiber," Opt. Lett. **38**, 3592–3595 (2013).
9. F. Couny, F. Benabid, and P. S. Light, "Large-pitch kagome-structured hollow-core photonic crystal fiber," Opt. Lett. **31**, 3574–3576 (2006).
10. Y. Y. Wang, N. V. Wheeler, F. Couny, P. J. Roberts, and F. Benabid, "Low loss broadband transmission in hypocycloid-core Kagome hollow-core photonic crystal fiber," Opt. Lett. **36**, 669–671 (2011).
11. D. J. Kane and R. Trebino, "Characterization of arbitrary femtosecond pulses using frequency-resolved optical gating," IEEE Journal of Quantum Electronics **29**, 571–579 (1993).
12. P. Bates, O. Chalus, and J. Biegert, "Ultrashort pulse characterization in the mid-infrared," Optics letters **35**, 1377–1379 (2010).
13. M. Miranda, C. L. Arnold, T. Fordell, F. Silva, B. Alonso, R. Weigand, A. L'Huillier, and H. Crespo, "Characterization of broadband few-cycle laser pulses with the d-scan technique," Opt. Express **20**, 18732–18743 (2012).
14. C. Iaconis and I. A. Walmsley, "Spectral phase interferometry for direct electric-field reconstruction of ultrashort optical pulses," Opt. Lett. **23**, 792–794 (1998).
15. P. Baum, S. Lochbrunner, and E. Riedle, "Zero-additional-phase SPIDER: full characterization of visible and sub-20-fs ultraviolet pulses," Opt. Lett. **29**, 210–212 (2004).
16. J. R. Birge, R. Ell, and F. X. Kärtner, "Two-dimensional spectral shearing interferometry for few-cycle pulse characterization," Opt. Lett. **31**, 2063–2065 (2006).
17. E. M. Kosik, A. S. Radunsky, I. A. Walmsley, and C. Dorrer, "Interferometric technique for measuring broadband ultrashort pulsesat the sampling limit," Opt. Lett. **30**, 326–328 (2005).
18. A. S. Wyatt, I. A. Walmsley, G. Stibenz, and G. Steinmeyer, "Sub-10 fs pulse characterization using spatially encoded arrangement for spectral phase interferometry for direct electric field reconstruction," Opt. Lett. **31**, 1914–1916 (2006).
19. T. Witting, D. R. Austin, and I. A. Walmsley, "Improved ancilla preparation in spectral shearing interferometry for accurate ultrafast pulse characterization," Opt. Lett. **34**, 881–883 (2009).
20. T. Witting, S. J. Weber, J. W. Tisch, and J. P. Marangos, "Spatio-temporal characterization of mid-infrared laser pulses with spatially encoded spectral shearing interferometry," Opt. Express **20**, 27974–27980 (2012).
21. S. Akturk, C. D'Amico, and A. Mysyrowicz, "Measuring ultrashort pulses in the single-cycle regime using frequency-resolved optical gating," JOSA B **25**, A63–A69 (2008).
22. K. Yamane, Z. Zhang, K. Oka, R. Morita, M. Yamashita, and A. Suguro, "Optical pulse compression to 3.4 fs in the monocycle region by feedback phase compensation," Opt. Lett. **28**, 2258–2260 (2003).
23. P. Londero, M. E. Anderson, C. Radzewicz, C. Iaconis, and I. A. Walmsley, "Measuring ultrafast pulses in the near-ultraviolet using spectral phase interferometry for direct electric field reconstruction," Journal of Modern Optics **50**, 179–184 (2003).
24. M. Kacprowicz, W. Wasilewski, and K. Banaszek, "Complete characterization of weak ultra-short near-uv pulses by spectral interferometry," Appl. Phys. B **91**, 283–286 (2008).
25. M. Hirasawa, N. Nakagawa, K. Yamamoto, R. Morita, H. Shigekawa, and M. Yamashita, "Sensitivity improvement of spectral phase interferometry for direct electric-field reconstruction for the characterization of low-intensity femtosecond pulses," Appl. Phys. B **74**, s225–s229 (2014).
26. F. Benabid, J. C. Knight, G. Antonopoulos, and P. S. J. Russell, "Stimulated raman scattering in hydrogen-filled hollow-core photonic crystal fiber," Science **298**, 399–402 (2002).
27. F. Benabid, F. Couny, J. Knight, T. Birks, and P. S. J. Russell, "Compact, stable and efficient all-fibre gas cells using hollow-core photonic crystal fibres," Nature **434**, 488–491 (2005).
28. F. Couny, F. Benabid, and P. Light, "Large-pitch kagome-structured hollow-core photonic crystal fiber," Opt. Lett. **31**, 3574–3576 (2006).
29. Y. Wang, N. V. Wheeler, F. Couny, P. Roberts, and F. Benabid, "Low loss broadband transmission in hypocycloid-core kagome hollow-core photonic crystal fiber," Opt. Lett. **36**, 669–671 (2011).
30. D. R. Austin, T. Witting, and I. A. Walmsley, "Broadband astigmatism-free czerny-turner imaging spectrometer using spherical mirrors," Appl. Opt. **48**, 3846–3853 (2009).
31. M. Anderson, L. de Araujo, E. Kosik, and I. Walmsley, "The effects of noise on ultrashort-optical-pulse measurement using spider," Appl. Phys. B **70**, S85–S93 (2000).
32. D. You and P. H. Bucksbaum, "Propagation of half-cycle far infrared pulses," J. Opt. Soc. Am. B **14**, 1651–1655 (1997).
33. E. Zeek, A. Shreenath, P. O'Shea, M. Kimmel, and R. Trebino, "Simultaneous automatic calibration and direction-of-time removal in frequency-resolved optical gating," Appl. Phys. B **74**, s265–s271 (2014).
34. A. Baltuska, M. S. Pshenichnikov, and D. A. Wiersma, "Second-harmonic generation frequency-resolved optical

#261180 Received 15 Mar 2016; revised 25 Apr 2016; accepted 25 Apr 2016; published 1 Jun 2016

gating in the single-cycle regime," IEEE J. Quantum Electron. **35**, 459–478 (1999).
35. G. Stibenz and G. Steinmeyer, "Interferometric frequency-resolved optical gating," Opt. Express **13**, 2617–2626 (2005).
36. F. Junginger, A. Sell, O. Schubert, B. Mayer, D. Brida, M. Marangoni, G. Cerullo, A. Leitenstorfer, and R. Huber, "Single-cycle multiterahertz transients with peak fields above 10 mv/cm," Opt. Lett. **35**, 2645–2647 (2010).
37. P. Malevich, G. Andriukaitis, T. Flöry, A. J. Verhoef, A. Fernández, S. Ališauskas, A. Pugžlys, A. Baltuška, L. H. Tan, C. F. Chua, and P. B. Phua, "High energy and average power femtosecond laser for driving mid-infrared optical parametric amplifiers," Opt. Lett. **38**, 2746–2749 (2013).
38. G. P. Agrawal, *Nonlinear Fiber Optics* (Academic, 2007).
39. J. Ratner, G. Steinmeyer, T. C. Wong, R. Bartels, and R. Trebino, "Coherent artifact in modern pulse measurements," Opt. Lett. **37**, 2874–2876 (2012).

1. Introduction

Single-cycle and sub-cycle laser waveforms play a critical role in attosecond technology because of the ability to confine a strong-field interaction to a single peak of the electric field [1–3]. Such temporal localization eliminates timing jitter with respect to the laser pulse envelope and ensures that the interaction is not recursive within one pulse. For example, sub-cycle pulses spanning 1.5-octave in the near infrared regime (350 nm to 1100 nm) revealed fine details of attosecond electron motion in krypton atoms within a single wave crest [3]. The generation of these extremely short field transients require careful dispersion control over ultra broadband spectral bandwidths. A suitable pulse characterization technique is a key component of such experiments. Ultrashort pulse characterization in the infrared (IR) spectral range is further complicated due to limitations in the spectral response of the detectors. The IR spectral region is attractive for numerous applications in pump-probe spectroscopy [4] and coherent extreme ultraviolet (XUV) radiation generation at higher photon energies [5, 6].

In this paper, we demonstrate the temporal characterization of a single cycle pulse source centered at 1700 nm with spectra spanning over one octave up to 2400 nm. The pulses are generated via the self-compression technique in a hollow core photonic crystal fiber filled with a noble gas as a nonlinear optical medium [7, 8]. The Kagome-lattice structure [9, 10] of the fiber leads to an extremely broad transmission bandwidth and high power handling and enables a compact sub-cycle, GW peak power source suitable for many strong-field applications. The characterization of these pulses is, however, not trivial due to extremely wide bandwidth, central wavelength lying in the IR spectral range and complex temporal intensity profile.

There are many techniques for ultrashort pulse characterization techniques, such as SHG-FROG [11, 12], d-scan [13] or interferometric techniques, the most prominent being spectral phase interferometry for direct electric-field reconstruction (SPIDER) [14]. Derivatives of SPIDER geared towards the accurate characterization of few-cycle pulses are the zero-additional-phase (ZAP)-SPIDER [15], two dimensional spectral shearing interferometry (2DSI) [16], and spatially encoded arrangement for SPIDER (SEA-SPIDER) [17, 18]. A variant of SEA-SPIDER that uses narrowband filters for the ancilla generation (SEA-F-SPIDER) has been shown to improve calibration of upconversion frequency and frequency shear leading to more accurate pulse measurements [19]. SEA-F-SPIDER has recently been adapted for the short-wave IR (SWIR) spectral range [20].

Our source of sub-cycle IR pulses is a nonlinear self-compression scheme first described in [7]. In this paper we present a cross SEA-F-SPIDER (X-SEA-F-SPIDER) pulse characterization setup developed for complete spatio-temporal characterization of octave-spanning IR pulses, where independent ancillae pulses pulses are derived directly from a near-IR (NIR) driving laser. We validate the suitability of our method of choice by comparing it to, and reaching the limit of another high-fidelity pulse characterization technique, SHG-FROG. In our X-SEA-F-SPIDER implementation we derive the ancillae beams from a different laser source at 1 µm wavelength. This enables us to shift the SPIDER sum-frequency signal (450-720 nm) of the IR

#261180 Received 15 Mar 2016; revised 25 Apr 2016; accepted 25 Apr 2016; published 1 Jun 2016

single-cycle test-pulses into a region of good spectral response of standard silicon based CCD cameras. Employing the X-SEA-F-SPIDER apparatus, we retrieved the details of the evolution of the soliton self-compression down to a single optic cycle in the IR wavelength range. We show pulse characterization results for various bandwidths of the self-compressed pulse and compare to the SHG-FROG [11] technique which fully reproduces the X-SEA-F-SPIDER results in the longer-pulse range. We discuss the requirements for pulse measurement methods when the pulse bandwidth is beyond one octave.

2. Technique of choice

The technique for single cycle pulse characterization in the IR range needs to meet a number of stringent requirements, such as support an over one octave bandwidth, add no additional dispersion to the test pulse, have no geometrical smearing limitations and employ suitable detectors. These limitations and challenges are discussed in detail in Section 5. Techniques that were not widely used in visible to near-IR spectral ranges become interesting for long wavelength pulse characterization.

Table 1. Comparison of Common Techniques for IR Single-cycle Pulse Characterization

Technique of choice	**SHG-FROG**	**X-SEA-F-SPIDER**
Spectral range	$\lambda < 2.2$ µm - Si detector $1.8 < \lambda < 4.8$ µm - InGaAs detector	λ only limited by SFG crystal, as the signal is up-converted to VIS range when mixed with NIR ancilla pulse
Instrument dispersion	split-mirror beam splitting required for dispersionless measurement or its dispersion has to be taken into account [33]	dispersion free
Type of measurement	time-frequency domain: time and spectral information is convoluted	frequency domain: spectral amplitude and phase measurements can be separated
Temporal accuracy	geometrical smearing ($\delta t \propto \lambda$, see section 5 for details)	no geometrical smearing
Bandwidth	up to one octave. Larger bandwidth for SHG FROG is possible using a non-collinear geometry, but results in geometrical smearing	more than one octave
Single shot detection	yes [21] (silicon based imaging detector can not be used for pulses with spectrum spanning beyond 2 µm)	yes
Spatio-temporal information encoding	no (limited access to the spatial information may be attained by aperturing different parts of the beam)	yes (along one spatial direction)
Susceptibility to noise	phase encoded into amplitude modulations of the signal	phase encoded into fringe positions

Table 1 compares the most relevant pulse characterization techniques SHG-FROG [21] with X-SEA-F-SPIDER, the latter one being particularly suitable for the over octave spanning pulse characterization in the IR range. SPIDER has been used for NIR few-cycle pulse characterization [22]. The X-SEA-F-SPIDER version described in this paper uses an ancilla derived directly from a NIR pump laser which is mixed with the test pulse. This situation is quite general as the

#261180 Received 15 Mar 2016; revised 25 Apr 2016; accepted 25 Apr 2016; published 1 Jun 2016

ultrashort IR pulses are typically generated via nonlinear frequency conversion of ultrafast NIR pump lasers in the 0.8-1 μm range. Using a quasi-monochromatic picosecond ancilla pulse derived from a small fraction of the pump laser pulse, the IR test pulse frequency is upconverted to the VIS range, conveniently accessible with silicon (Si) detectors. The X-SEA-F-SPIDER technique described here allows measurements of over one octave broadband pulses in the IR range, is free from geometrical smearing effects, adds no additional dispersion to the test pulse and allows single shot acquisition. The measured spectral phase and spectral intensity are decoupled from each other and allow independent cross-checks with a directly measured pulse spectrum. In addition, it provides temporal profile information across one spatial coordinate, which is useful for monitoring possible spatio-temporal distortions of the pulse.

The X-SEA-F-SPIDER scheme presented here, where the ancillae pulses are derived directly from a laser source and are independent on the pulse that is being tested, was previously analysed in the context of ultraviolet (UV) pulse characterization [23, 24] and sensitivity improvement [25]. The frequency up-conversion or down-conversion approach using an appropriate probe pulse is closely related to the cross-FROG (XFROG) technique. In the XFROG scheme it is possible to mix the test pulse with a higher frequency probe pulse so that the signal is frequency-upconverted to the spectral range compatible with the detector. However, this approach has limitations inherent to the time-domain measurement - the spatial smearing and requires ultrashort probe pulses, with the duration comparable to the test pulse. These issues are discussed in depth in section 5.

3. Experimental setup

The pulse self-compression and X-SEA-F-SPIDER characterization optical setup is summarized in Fig. 1. It consists of a femtosecond laser pumped OPA, a Kagome HC-PCF (Hollow core photonic crystal fiber) enclosed in a gas cell and the X-SEA-F-SPIDER and SHG-FROG apparatuses for pulse characterization.

A femtosecond Ytterbium Chirped Pulse Amplifier (Yb CPA) delivering 190 fs, 1030 nm pulses at 6 W average power is employed as a front-end for pumping of the IR-optical parametric amplifier (IR-OPA). Yb laser technology allows rather efficient power up-scaling due to direct diode pumping and the low quantum defect. The wavelength of the IR-OPA is tunable in the 1380 nm-2000 nm range for the signal pulse and 2000 nm-4000 nm for the idler pulse. Pulses from the OPA at 1800 nm central wavelength and nearly transform limited 80 fs full width at half maximum (FWHM) pulse duration are coupled into the Kagome HC-PCF [26–29], which is fixed in a gas cell and filled with noble gas (xenon, krypton, argon or neon) that acts as a nonlinear medium. The dispersion estimation of the HC-PCF shows that under our experimental conditions (argon, <3 bar) the total dispersion of the waveguide including gas is anomalous in the spectral range above 1100 nm.

The near-single-cycle pulses are generated upon nonlinear propagation that leads to a near 20-fold shortening of the pulse envelope. At a certain input power of the pulse the negative waveguide dispersion balances the positive chirp due to self-phase modulation (SPM) and leads to self-compression of the pulse. The nonlinear phase shift ($\triangle n_{nonlinear} \sim n_2 I$, n_2 is the nonlinear refractive index of the gas medium, and I is the laser intensity) can be controlled by changing the input pulse energy, the pressure and type of the filling gas. By optimising the input pulse energy, central wavelength, gas type and pressure, the shortest pulse transient is generated at the end of the fiber. Further increase of the pulse energy leads to the breakup of the pulse into several sub-pulses of smaller peak power. The availability of reliable characterization tools for this ultrabroad bandwidth is necessary for optimization of these parameters. By optimizing the control parameters (fiber length, input pulse energy, gas type and pressure), a pulse with a spectrum spanning from 900 nm to 2400 nm, corresponding to a sub-cycle transform-limited pulse

#261180 Received 15 Mar 2016; revised 25 Apr 2016; accepted 25 Apr 2016; published 1 Jun 2016

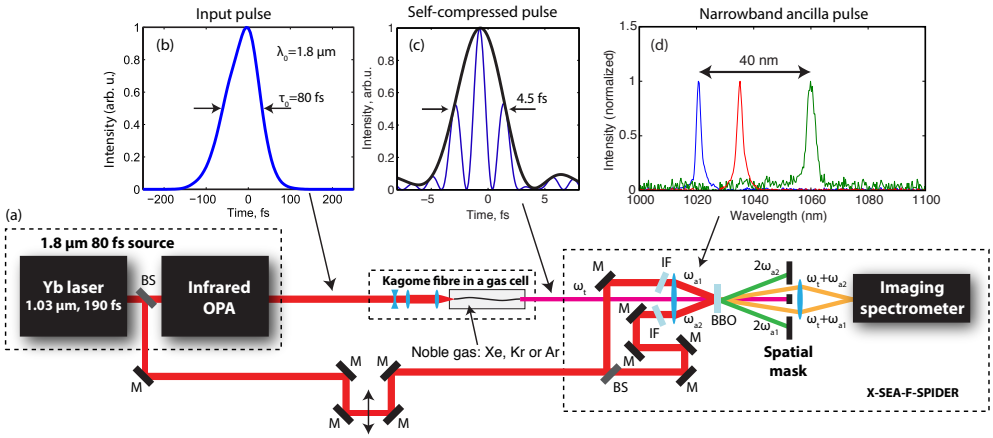

Figure 1. (a) Scheme of the experimental setup for IR pulse self-compression in Kagome fiber and pulse characterization using X-SEA-F-SPIDER. IF - interference filter, BS - beam splitter, M - mirror, $\omega_{a1,a2}$ are ancillae pulse frequencies, ω_t is the test pulse central frequency, and $\omega_t + \omega_{a1,a2}$ are the sum-frequency beams. Note that the lens after the Kagome fiber is shown in order to simplify the drawing, the actual setup uses dispersionless spherical focusing mirror for re-imaging the beam onto the crystal; (b) input pulse profile; (c) measured single-cycle self-compressed pulses. Black curve denotes the pulse envelope, the blue curve - square of the instantaneous electric field; (d) spectra of narrowband ancillae pulses at different interference filter angles, spectra are individually normalized.

duration, can be generated at the output of the fiber.

These pulses are characterized using an adapted X-SEA-F-SPIDER setup, based on the further enhanced instrument presented in [20]. The scheme presented in this paper has two key new features: (1) the ancilla pulse is derived from the driving laser and is independent of the test pulse, which allows convenient varying of self-compression parameters without affecting the measurement apparatus; (2) the ancilla pulse wavelength is significantly shorter than the test pulse which allows measuring pulses further into the IR range as the sum-frequency signal between an IR test-pulse and ancilla pulse at 1 μm lies in the responsive region of standard silicon CCD cameras. Two quasi-monochromatic frequency sheared ancillae pulses are prepared by splitting off two beams of a small fraction of the pump laser pulse centered at 1030 nm and passed through narrowband filters (3 nm bandwidth). The central wavelength of the transmission window of the interference filters can be tuned within a 40 nm range by rotating the angle of incidence of the interference filters. The tuning range is limited mainly by the bandwidth of the 1030 nm pulse as shown in panel (d) of Fig. 1. The filter transmission window at normal incidence is centered at 1064 nm and shifts towards the shorter wavelength side when rotated at an angle.

The test pulse and the two ancillae beams are focused into a thin BBO ($L = 20\,\mu$m) crystal for sum-frequency mixing in a non-collinear geometry as shown in Fig. 1. The phase-matching bandwidth of our BBO crystal (type-I phase matching) in this spectral range is sufficiently broad to support octave-spanning sub-cycle pulse spectra. During the sum-frequency generation, the whole test pulse spectrum is up-converted to the visible range with the same bandwidth $\Delta\omega$ as illustrated in Fig. 6. However, note that the relative bandwidth $\Delta\omega/\omega_0$ is much smaller due to increased central frequency. For example, a test pulse with a spectrum spanning from 1000 nm to 2400 nm is upconverted by a quasi-monochromatic ancilla centered at 1030 nm to a sum-frequency spectrum spanning only from 500 nm to 700 nm in the visible spectral range.

#261180 Received 15 Mar 2016; revised 25 Apr 2016; accepted 25 Apr 2016; published 1 Jun 2016

This spectral range is compatible with the well established low noise silicon based CCD detectors. The two generated sum-frequency beams are separated in space between the two ancillae beams. They are spatially filtered using a mask consisting of beam apertures as shown in Fig. 1 and imaged onto the entrance slit of a 2D imaging spectrometer [30].

Figure 2 illustrates the 2D imaging spectrometer and reconstruction procedure. The two two frequency-sheared beams E_1 and E_2 are re-imaged with slight magnification onto the slit of the imaging spectrometer [30]. Due to the astigmatism free design the fringe interference pattern created in the BBO crystal is finally re-imaged onto the CCD image plane where the spectrum is dispersed. A CCD camera (640 × 480 pixel, 14 bit, AVT GmbH) is used to record the interferogram. The SPIDER interferogram as shown in Fig. 2 panel (c), consists of a non-modulated intensity term DC term ($|E_1|^2 + |E_2|^2$) and a modulated AC term ($|E_1||E_2|\cos(\varphi(\omega) - \varphi(\omega - \Omega) + \Delta K) = |E_1||E_2|\cos(\Delta\varphi(\omega) + \Delta K)$), where $\varphi(\omega)$ and $\varphi(\omega - \Omega)$ are the phase of E_1 and E_2, Ω is the frequency shear, ΔK is the propagation vector difference due to angle between the beams, and the group delay is encoded in the phase difference $\Delta\varphi(\omega)$. In additional, a calibration interferogram is also recorded (panel (d)) by setting the ancillae pairs to the same frequency. From this calibration interferogram the term ($|E_1||E_2|\cos(\Delta K)$) can be extracted. The AC terms are separated from the DC term in the Fourier domain, and one AC term sideband can be selected by numerical filtering. The noise distributed outside the filter range will be removed which drastically improves the signal-to-noise ratio making SPIDER very resilient against noise [31]. In order to obtain the desired phase information, we subtract the calibration phase to obtain the spectral phase difference $\Delta\varphi(\omega)$. The desired spectral phase $\varphi(\omega)$ can be obtained by integrating the phase difference $\varphi(\omega) = \int \Delta\varphi(\omega)\mathrm{d}\omega/\Omega$, thus the full temporal profile information distribution across one spatial coordinate is reconstructed.

#261180 Received 15 Mar 2016; revised 25 Apr 2016; accepted 25 Apr 2016; published 1 Jun 2016

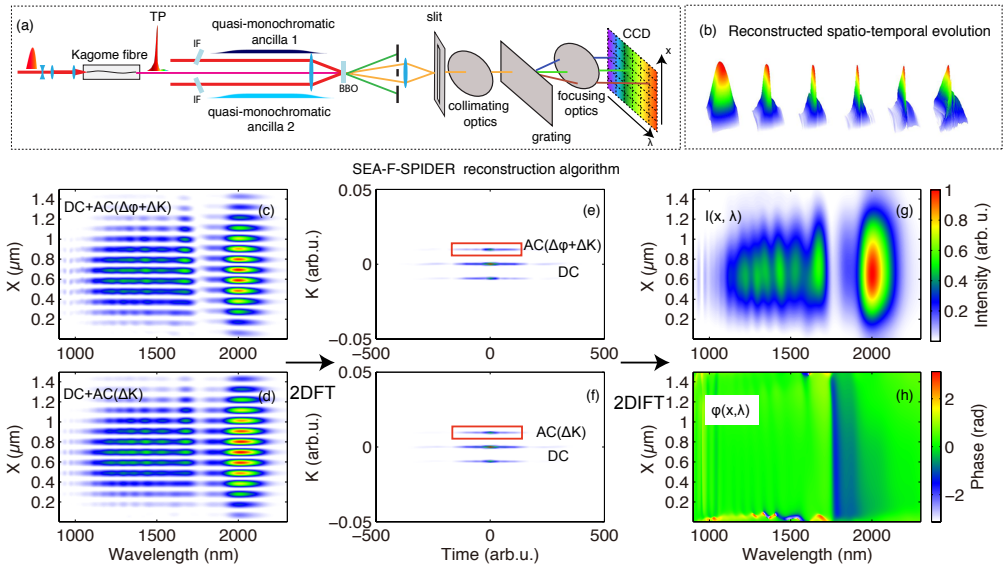

Figure 2. Scheme of pulse reconstruction via Fourier analysis of the captured interferogram. IF, interference filter, TP, test pulse; (a) geometry of the experiment and the 2D imaging spectrometer; (b) reconstructed spatio-temproal profile evolution with increasing input pulse energy; (c) X-SEA-F-SPIDER trace with frequency-sheared ancillae pair; (d) X-SEA-F-SPIDER calibration trace with the same frequency ancillae pair; (e) and (f) are the 2D Fourier transforms of (c) and (d) and illustrates the separation of the AC and DC terms; (e) and (f) are the reconstructed spectral intensity and phase across the spatial coordinate x.

Here we show that the X-SEA-F-SPIDER characterization apparatus is able to characterize sub-cycle pulse transients, even though such broadband pulses can not freely propagate as a consequence of the Gauss theorem [32]. As shown in Fig. 3, once the sub-cycle transient forms right at the output of the HC-PCF, longer wavelength components diverge faster than the blue ones which effectively narrows the spectrum at every point across the beam and thus the pulse duration increases even in non-dispersive media. In other words, it can be considered as a group of few cycle pulses propagating with locked phase. The re-imaging by a spherical mirror leads to constructive addition of the different color components forming a sub-cycle transient at the image plane. The interference pattern formed by the two sum-frequency beams of the sub-cycle transient with two frequency-sheared ancillae pulses is again re-imaged to the entrance slit of the imaging spectrometer, which allows reconstructing the full spatio-temporal structure of the sub-cycle transient.

#261180 Received 15 Mar 2016; revised 25 Apr 2016; accepted 25 Apr 2016; published 1 Jun 2016

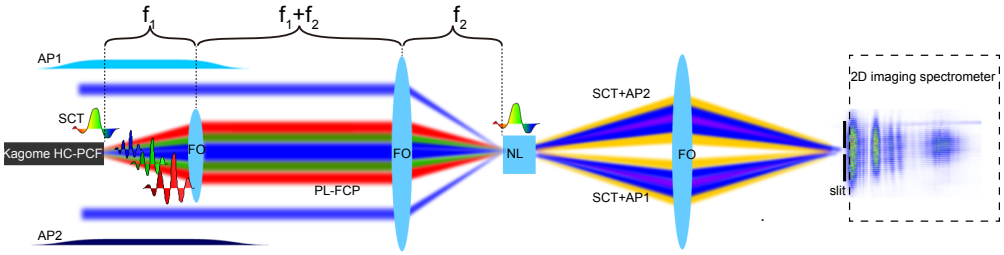

Figure 3. The sub-cycle transient structure can be reconstructed using a re-imaging geometry. SCT, sub-cycle transient, PL-FCP, phase locked few cycle pulses, AP1 and AP2 are the ancillae pairs, FO, focusing optics, NL, nonlinear crystal, SCT+AP1 and SCT+AP2 are sum-frequency beams between sub-cycle test pulse and the ancillae.

4. Comparison of X-SEA-F-SPIDER and SHG-FROG measurement results

In the solitonic self-compression process, the short pulse is formed at a specific distance in the HC-PCF depending on gas nonlinearity, pressure, input pulse energy, fiber diameter and dispersion. The easily variable parameter for the optimization of the minimum pulse duration at the output is pulse energy rather than the fiber length. We scan the launched pulse energy into the HC-PCF and measure temporal profiles using both the X-SEA-F-SPIDER and FROG techniques. The SHG-FROG measurement allows comparing and cross-checking the measurement fidelity of the X-SEA-F-SPIDER results in the range where the pulse spectrum is significantly narrower than one octave.

The reconstructed spectral and temporal profiles obtained using both methods for different input pulse energies are shown in Fig. 4. In the multi-cycle regime (panels (a) and (b)) the spectrum broadens nearly symmetrically and the pulse self compresses to shorter duration due to the self-phase-modulation in the presence of anomalous waveguide dispersion. Not only pulse duration, but also the shapes of temporal profile and group delay show nice agreement from these two methods. However, when the IR pulse shortens down to the single cycle regime (panel (c) and (d)), we find that the issues related to octave spanning spectrum measurements (i.e. geometrical smearing, SH pulse spectrum overlaps with fundamental) become critical as discussed in detail in the following section.

5. Limitations of pulse measurement techniques

Here we would like to address the few issues that reduce the measurement accuracy in SHG-FROG and compare it to the X-SEA-F-SPIDER technique. When the pulse is shorter than two optical cycles ($\approx$ 10 fs), the beam-splitter induced dispersion becomes significant. While this issue can be removed by employing split-mirror beam splitter, this creates many new issues if the spatial profile is not perfectly uniform. In our X-SEA-F-SPIDER apparatus (Fig. 1), the self-compressed sub-cycle test pulse at the output of the fiber is re-imaged onto the sum-frequency-generation (SFG) crystal using spherical focusing mirrors with no additional dispersion. Although it is possible to take into account the phase introduced by beam-splitter numerically or even use an asymmetric scheme in SHG-FROG where one pulse is transmitted through beam splitter and the other one is reflected without added dispersion [33], this requires sophisticated reconstruction algorithms and limits the reliability of the measurement for ultrabroadband pulses with complex temporal structure.

Another problem associated with the SHG-FROG measurement of IR pulses is that the silicon spectrometer response drops rapidly above 1 μm. We have measured and calibrated

#261180 Received 15 Mar 2016; revised 25 Apr 2016; accepted 25 Apr 2016; published 1 Jun 2016

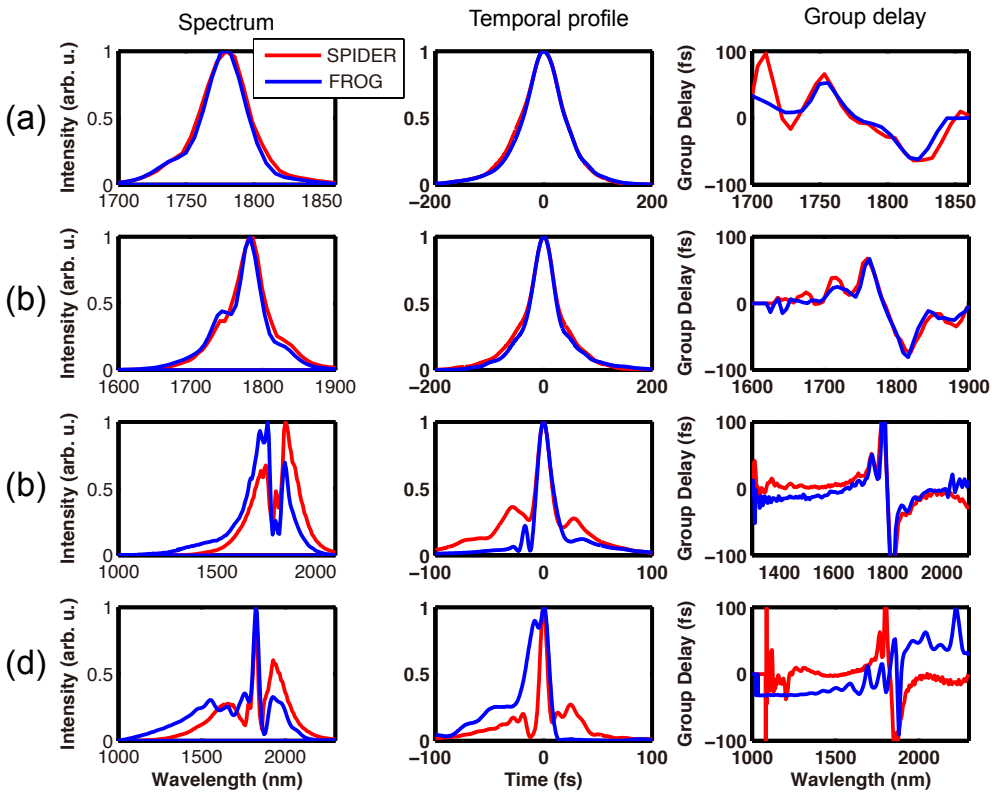

Figure 4. Spectral temporal characterization comparison between SHG-FROG and X-SEA-F-SPIDER from multi-cycle to single cycle regime. Left column: spectrum, middle column: temporal profile, right column: group delay. In case of SPIDER, frequency-shifted spectra obtained from the imaging spectrometer are shown.

the FROG traces by compensating the CCD response, diffraction grating and fiber transmission spectrum against a black body calibration lamp, however, in practice, it is not possible to correct arbitrary low responses due to the limited dynamic range of the detector. We find the measurement accuracy to be reduced as soon as the red wing of the spectrum spans beyond 2000 nm. As shown in the Figs. 4(c) and 4(d), the test pulse spectrum broadens further to longer wavelengths at higher input pulse energies and the second-harmonic signal reaches already beyond the silicon detector response range ($\approx$ 1100 nm) resulting in significant inaccuracy of the FROG retrievals. Simultaneous use of a silicon spectrometer and a thermoelectrically cooled InGaAs spectrometer may solve this problem at the expense of an increased complexity of the system and reduction of the accuracy of the measurement. In contrast, in our implementation of X-SEA-F-SPIDER the signal is shifted from the IR to the visible spectral range, where the silicon detector response is much higher as illustrated in Fig. 6.

The spectral range limitation of FROG apparatus mentioned above can be solved in a XFROG scheme by mixing the test pulse with a higher frequency probe pulse so that the signal is frequency-upconverted to the spectral range compatible with the detector. However the XFROG approach requires short probe pulses, with the duration comparable to the duration of the test pulse, in order to work with suffcient accuracy. In an experimental configuration, where the pulse duration of the driving laser is many times longer than the test pulse to be measured, this would yield unacceptably large measurement errors. This limitation is not applicable in

#261180 Received 15 Mar 2016; revised 25 Apr 2016; accepted 25 Apr 2016; published 1 Jun 2016

X-SEA-F-SPIDER, because here a narrowband ancillae pulses are needed. For example, for the 4.5 fs pulse characterization experiments a $\lambda = 1\,\mu$m 200 fs pump laser was used.

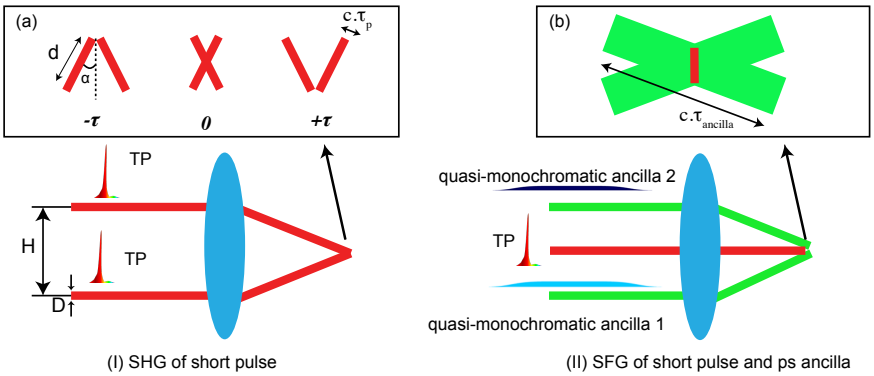

Figure 5. Comparison of geometric time smearing effects between SHG-FROG and X-SEA-F-SPIDER techniques in the IR single-cycle regime. (I) is the case of non-collinear SHG-FROG, TP are the two replicas of the short test pulses, D is the beam size, and H is the separation distance. Inset (a) shows pulse front overlap at $-\tau$ (where the pulses start to overlap), 0 and $+\tau$ time delays in the focal plane where the two beams cross. d is beam diameter at the focus, and θ is half of the intersection angle of the two beams. The spatial length of the fs pulse is $c\tau_p$, c is speed of light and τ_p is pulse duration. (II) is the case of sum frequency generation in X-SEA-F-SPIDER. TP is the short test pulse, AP1 and AP2 are the two ps ancillae; inset (b) illustrates that the time smearing is absent in the focal plane due to the long durations of the ancillae pulses fully overlapping with the test pulse and no temporal scanning involved.

Furthermore, the ultimate temporal accuracy limitation of non-collinear SHG-FROG and XFROG is the geometric time smearing effect, $\tau_m^2 = \tau_p^2 + \delta t^2$, where τ_m, τ_p are measured and ideal FWHM pulse duration, and δt is the time smearing due to the intersection of non-collinear beams [34]. As illustrated in the Fig. 5, in the case of non-collinear SHG-FROG, for a range of times, the two short test pulse beams cross each other in the focal plane, ultimately resulting in longer measured pulse duration. This time smearing can be written as $\delta t = \alpha d/c$, where d is the beam diameter in the focal plane and α is the intersection half-angle of the two beams. We consider two Gaussian beams separated by distance H, with beam diameter D, and the focal length of the focusing optics is f. In this case, $\alpha = H/(2f)$, and beam diameter in the focal plane is $d = f\lambda/(\pi D)$. As a result, the time smearing can be further written as $\delta t = (H\lambda)/(D2\pi C)$, where λ is the central wavelength of the pulse to be measured. Here, one can see that the time smearing inaccuracy increases with increasing wavelength. Under our typical conditions ($H = 1$ cm, $d = 2$ mm), the time smearing effect leads to a 0.7 fs inaccuracy for a 10 fs pulse, and 1.4 fs for a 5 fs pulse at 1500 nm wavelength. In contrast, X-SEA-F-SPIDER is free of geometric time smearing, because the entire test pulse is fully overlapped with a narrow-band picosecond ancilla pulse. Again, this issue can be solved with interferometric FROG [35], but the measurement time is substantially increased because it requires very fine scanning steps and is not suitable for more dynamic experimental conditions as the pulse shape might change substantially during the measurement time. In addition, interferometric FROG still is not suitable for spectra spanning over one octave because the second harmonic signal of the red wing of the pulse overlaps with the blue wing of the fundamental pulse.

One limitation inherent to all second-order pulse characterization techniques is the phase matching bandwidth and frequency-dependent conversion efficiency. The measured signal can

#261180 Received 15 Mar 2016; revised 25 Apr 2016; accepted 25 Apr 2016; published 1 Jun 2016

be written as a product of a spectral filter term due to phase matching and an ideal nonlinear response term ($I_i(\omega)$): $I_m(\omega) \propto R(\omega)I_i(\omega)$. This distortion can be circumvented by using a very thin crystal [34]. Figure 7 shows the conversion efficiencies (phase matching term $R(\omega)$) calculated for different crystals. For example, let us assume the test pulse spectrum spans from 1 μm to 2 μm. A BBO nonlinear crystal (θ=20 deg, type I) of 20 μm thickness provides enough bandwidth over the range used in our experiment (from 500 nm to 666 nm in the sum frequency).

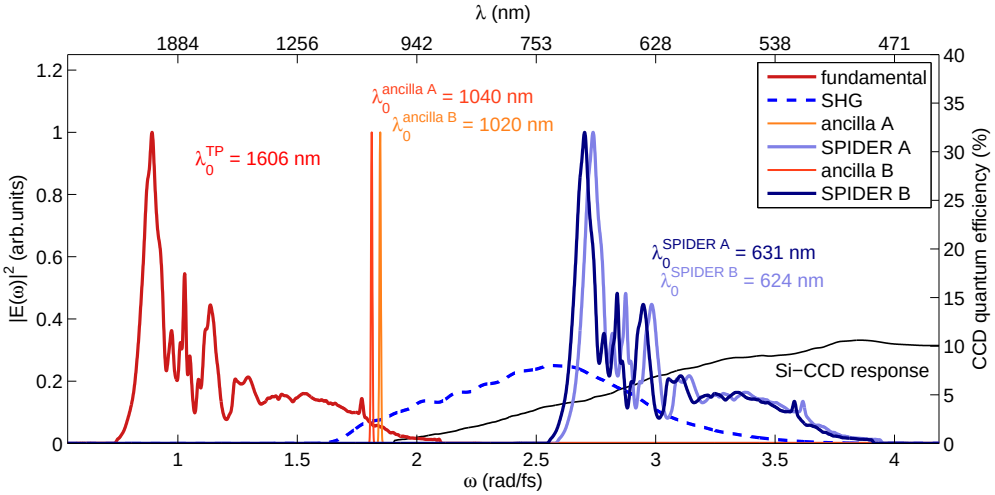

Figure 6. Up-conversion of pulse spectrum in X-SEA-F-SPIDER and comparison to the corresponding SHG spectrum in case of SHG-FROG measurement (dashed blue line). The SHG signal was calculated assuming perfect phase matching. The red curve is one measured over octave spanning spectrum at central wavelength of 1606 nm, frequency-sheared quasi-monochromatic ancillae pair is centered at 1040 nm (red) and 1020 nm (orange), the two sum-frequency spectra are shown with dark and light blue curves; the corresponding central wavelengths of the up-converted pulses are 631 nm and 624 nm respectively. Note that the SFG preserves fine spectral features of the test pulse, while SHG washes those out in case of Fourier-limited pulse.

Sub-cycle pulses inherently contain bandwidths wider than one octave. Such a wide relative bandwidth is challenging to characterize due to the varying response of detectors. In case of SHG-FROG the nonlinear response is the auto-convolution of the fundamental spectrum: $I_i(\omega) = I_t(\omega) * I_t(\omega)$ and yields an increase of the bandwidth $\Delta\omega \rightarrow 2\Delta\omega$. In a collinear SHG-FROG case this would lead to the overlapping of the second harmonic of the red wing with the blue wing of the fundamental spectrum. This issue does not apply to the X-SEA-F-SPIDER case where the signal retains the bandwidth of the test pulse, but at higher carrier frequency which brings it to the spectral range where typical detectors have much flatter response functions. In fact, the relative bandwidth of the signal is even reduced ($\Delta\omega/\omega_t \rightarrow \Delta\omega/(\omega_t + \omega_a)$). As an example, Fig. 6 shows the frequency upconversion of an over octave spanning test pulse spectrum by sum-frequency generation with the quasi-monochromatic frequency sheared ancillae pairs. The resulting sum-frequency spectrum is reduced to a bandwidth of below one octave at the new central frequency.

Another practical advantage of the X-SEA-F-SPIDER scheme is that it allows efficient filtering of the unwanted stray light and background (i.e. due to scattering in optical elements) in the measured interferogram as the signal is spatially modulated and can be isolated in the spatial-frequency Fourier domain.

#261180 Received 15 Mar 2016; revised 25 Apr 2016; accepted 25 Apr 2016; published 1 Jun 2016

6. Extension to longer wavelengths

The X-SEA-F-SPIDER technique, where the ancilla pulse is derived directly from a NIR laser, can be used with pulses with wavelengths well beyond 2.4 μm in the mid-wave IR (mid-IR) range. Typically ultrashort mid-IR pulses are generated via nonlinear frequency conversion starting from NIR pump lasers, i.e. Ti:Sapphire operating at 0.8 μm [20] or Yb doped media operating at around 1 μm. Using a NIR ancilla pulse derived from the NIR laser, the mid-IR test pulse is up-converted to the VIS spectral range, easily accessible by the well-developed high signal-to-noise ratio (SNR) Si detectors. Figure 7 summarizes usable nonlinear crystals for SFG with phase-matching bandwidth in the 1-12 μm range when the mid-IR test pulse is mixed with a 1 μm ancilla pulse (i.e. derived from an Yb pump laser). The yellow line corresponds to the characterization of pulses up to 2.4 μm using type-I phase matching in a BBO crystal as described in Section 7. Note that type-II interaction in BBO yields an even broader phase matching bandwidth (green curve in Fig. 7) in this spectral range. For further scaling of the wavelength different crystals need to be used for SFG as BBO is limited by the onset of absorption beyond 2.5 μm. Single cycle pulse generation in the THz to mid-IR range via DFG [36] was demonstrated and few-cycle OPCPA/OPA systems in the 6 μm range are being developed [37] showing the necessity of reliable pulse characterization methods in this spectral range. Gallium Selenide (GaSe) crystals are a particularly attractive option for SFG in this spectral range as shown by the blue and red phase matching curves in Fig. 7. Note that despite the long wavelength of the test pulse, the up-converted test pulse spectrum always lies in the VIS/NIR spectral range (500nm to 900nm) where the response of standard silicon based CCD cameras is relatively flat as shown in the panel (a) of Fig. 7.

#261180 Received 15 Mar 2016; revised 25 Apr 2016; accepted 25 Apr 2016; published 1 Jun 2016

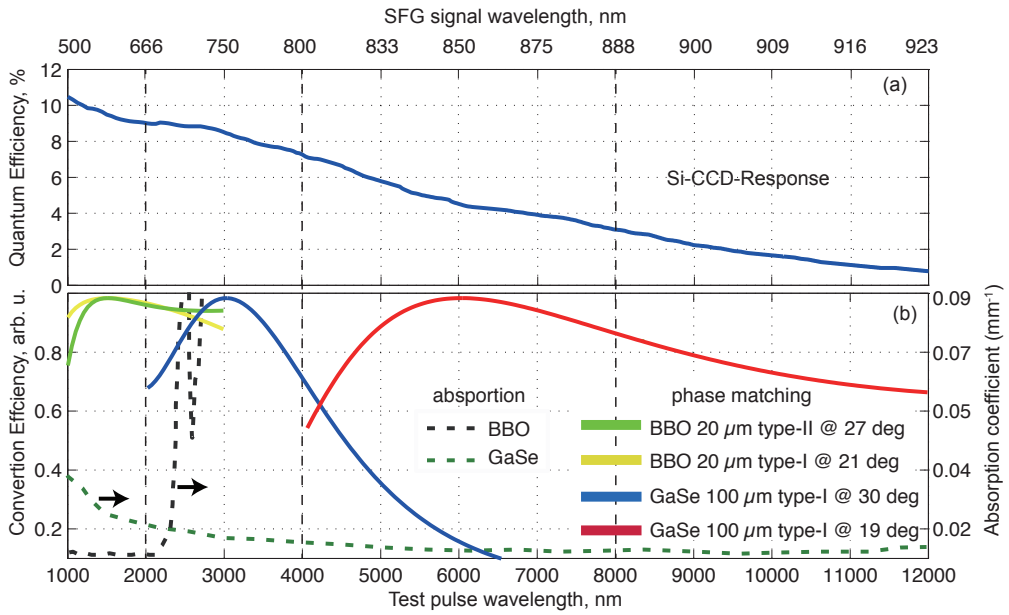

Figure 7. Phase-matching calculation for SFG of mid-IR test pulses with quasi-monochromatic 1000 nm ancillae pulses using BBO and GaSe crystals in different spectral ranges; (a) response of a Si CCD detector for corresponding up-converted signal wavelengths in the visible range; (b) the phase matching filter curves in different spectral ranges for 20 μm BBO and 100 μm GaSe nonlinear crystals at different phase-matching angles θ. Dashed curves show the absorption of the two crystals. The vertical dashed lines indicate that the spectral range spans 3 octaves: 1000 nm-2000 nm, 2000 nm-4000 nm and 4000 nm-8000 nm.

7. Pulse measurement in the single-cycle regime

As summarized in section 5, the X-SEA-F-SPIDER method is particularly suitable for octave-spanning pulse characterization in the IR spectral range. In order to demonstrate its capabilities for the characterization of shortest pulses, we optimized the experimental conditions of pulse self-compression for the generation of shortest pulse durations [7]. While the measurements presented in Fig. 4 allow a direct comparison between the SHG-FROG and the X-SEA-F-SPIDER techniques, the following measurement shows the ability of the X-SEA-F-SPIDER apparatus to characterize pulses with octave-spanning spectra. For this we used a shorter Kagome fiber (20-cm) and higher nonlinearity filling gas (3 bar xenon) in order to increase the self-compressed pulse bandwidth to more than one octave at a certain input pulse energy. Figure 8 presents the measured X-SEA-F-SPIDER traces recorded using the 2D imaging spectrometer at three different input pulse energies. Even in the most broadband pulse case spanning from 900 nm to 2400 nm, the corresponding sum-frequency signal wavelength spans only from 450 to 720 nm where the response of the silicon CCD detector is relatively good. These measurements show that the over octave spanning spectrum with potentially sub-cycle duration can be measured using X-SEA-F-SPIDER technique.

#261180 Received 15 Mar 2016; revised 25 Apr 2016; accepted 25 Apr 2016; published 1 Jun 2016

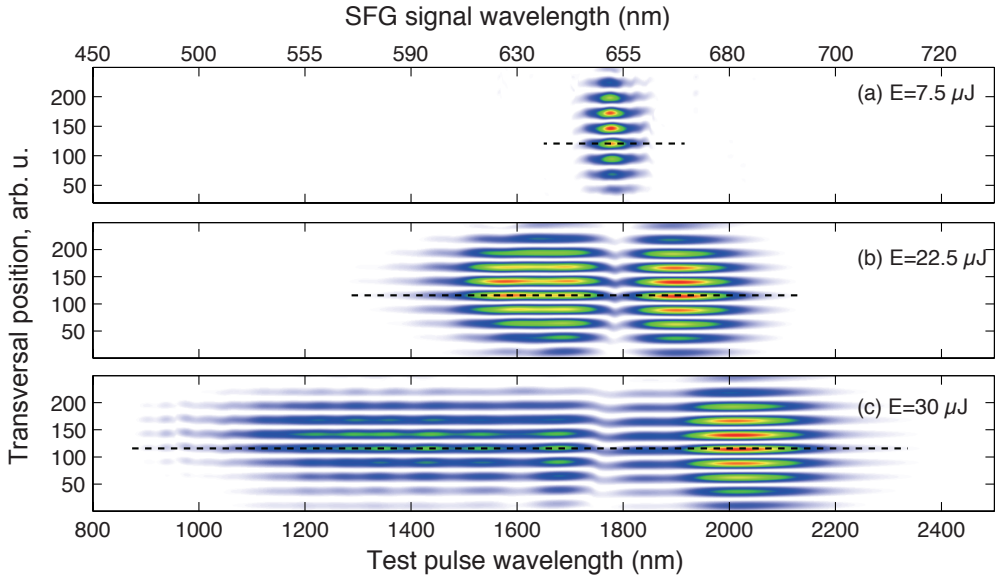

Figure 8. Measured X-SEA-F-SPIDER traces for three different input pulse energies and corresponding pulse widths. Pulses were self-compressed in 20 cm long fiber filled with 3 bar xenon. The input energies correspond to different stages of pulse self-compression in Kagome fiber: (a) the lowest 7.5 μJ input energy case where the pulse spectrum broadening is negligible (b) the intermediate energy case of 26 μJ, where a short 16 fs transient is being formed, and (c) at the input energy of 35 μJ, the ultra-short 5 fs pulse is formed. The horizontal dashed line is a guide for the eye corresponding to the constant group delay. Spatial Fourier filtering was applied for removing the background from the data.

The frequency-dependent group delay (GD) is encoded in the contours of the fringe pattern ($\mathrm{GD}(\omega) \propto x_0(\omega)$, where $x_0(\omega)$ is the peak or zero of the fringe). Straight fringes across the pulse spectrum indicates constant group delay and therefore, a transform-limited pulse. In case of a wide spectrum as shown in Fig. 8 (b,c), the range of well-compressed spectral portions of the pulse can be found by comparing the group delay to the horizontal line (a guide to the eye). The general trend is that most of the spectral content of the pulse has constant group delay (temporally compressed) and only the part around the initial input pulse wavelength has some distortion. These distortions are intrinsic for self-compression and lead to the appearance of a pulse pedestal in the time domain [38].

Employing X-SEA-F-SPIDER, we can retrieve the details of the soliton self-compression evolution. Figure 9 illustrates the evolution of spectrum, temporal profile, pulse duration and pulse fidelity for different input pulse energies, which can be separated into three stages. In the first stage, the spectrum broadens nearly symmetrically and the pulse self-compresses to a shorter duration ($\approx$ 20 fs FWHM). In the second stage (input pulse energy above 20 μJ), the pulse shortens down to few cycle duration (<10 fs), the self-steepening effect leads to a significant temporal shock wave formation with a longer leading front and a steeper trailing edge of the pulse. In the spectral domain, this corresponds to the highly asymmetric spectrum that has a long extension towards to short wavelengths. When the input pulse energy is increased to 32 μJ, the self-compressed pulse spectrum very rapidly broadens to an impressive width spanning from 900 nm to 2400 nm. In the time domain this corresponds to self-compression of the pulse down to nearly single cycle duration (5.5 fs) with more than 50% energy concentrated in the main peak. When the input pulse energy is increased even more, a very short light transient

#261180 Received 15 Mar 2016; revised 25 Apr 2016; accepted 25 Apr 2016; published 1 Jun 2016

(down to 4.5 fs) is formed right at the exit of the fiber with the envelope duration shorter than the field cycle. Here the pulse is on the edge of the soliton break up, which marks the third and undesirable stage, when the pulse fidelity drops rapidly and the pulse starts to split into a train of chaotic pulses. The pulse fidelity Q here refers to the fraction of the energy in the main peak of the pulse and is defined as:

$$Q = \frac{E_{Gauss}}{E_{pulse}} = \frac{P_0 \int_{-\infty}^{+\infty} \exp(-4\ln 2 t^2/\tau_{\text{fwhm}}^2) dt}{\int_{-\infty}^{+\infty} P(t) dt} = \frac{P_0 \sqrt{\pi} \tau_{\text{fwhm}}/(2\sqrt{\ln 2})}{\int_{-\infty}^{+\infty} P(t) dt} \quad (1)$$

where E_{Gauss} is the energy of a Gaussian pulse of the same duration τ_{fwhm} and peak power P_0 as the measured pulse profile $P(t)$.

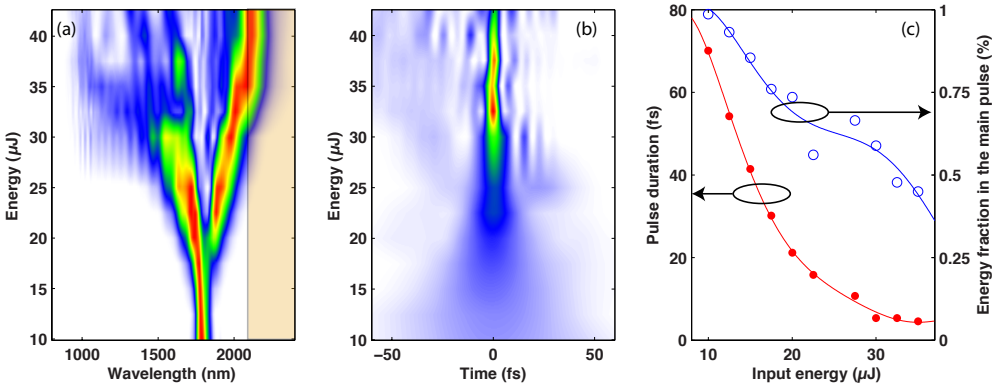

Figure 9. Soliton self-compression evolution as a function of input pulse energy, characterized using X-SEA-F-SPIDER. (a) spectrum, the second harmonic of the shaded area part of the spectrum is beyond the silicon detector working range ($\approx$ 1100 nm) (b) temporal evolution, (c) pulse duration and energy fraction in the main pulse as defined in Eq. (1).

Figure 10 illustrates the pulse spatio-temporal structure obtained from X-SEA-F-SPIDER in the single-cycle and sub-cycle regime (panel (a) and (c)). The pulse duration and energy fraction in the main pulse [Eq. (1)], referred to as pulse fidelity, across the spatial coordinate are shown in panels (b) and (d). The curvature and tilt of the pulse front was removed in the plots (the arrival time of the peak intensity was set to zero for all positions across the beam) and only the pulse profile is shown. At higher input pulse energy (panel (c), (d)), a second satellite peak emerges, and the pulse fidelity drops below 50%, while a sub-cycle transient (4.5 fs) is formed. The spatio-temporal information allows precise optimization of experimental parameters for shortest pulse duration and uniform pulse profile across the beam.

#261180 Received 15 Mar 2016; revised 25 Apr 2016; accepted 25 Apr 2016; published 1 Jun 2016

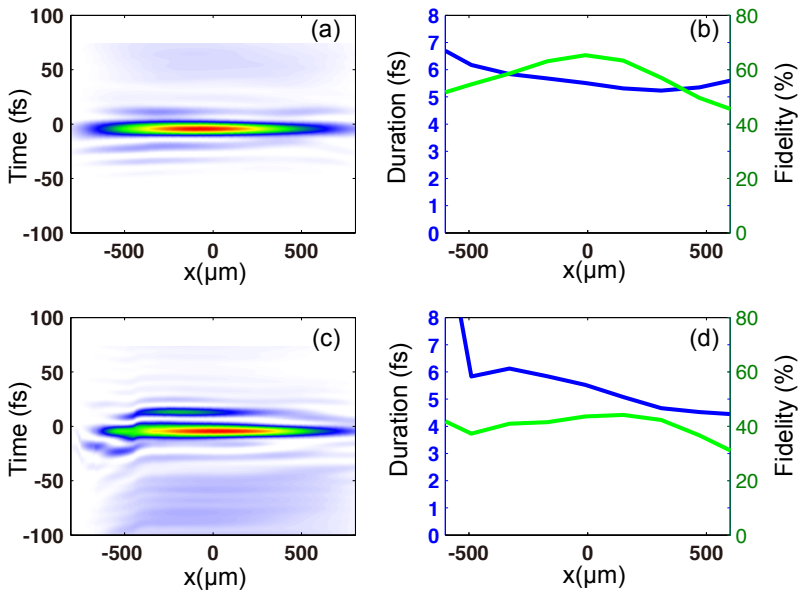

Figure 10. Spatio-temporal structure and pulse duration (FWHM), pulse fidelity [Eq. (1)] across the beam at single cycle (a), (b) and sub cycle regime (c), (d). The magnification factor of the re-imaging optics is ≈ 20.

8. Conclusion

Development of single and even sub-cycle pulse sources in the IR range is attractive for many strong-field and attosecond physics applications. Optimization and generation of these pulses require reliable pulse characterization methods. In this work, we have demonstrated a X-SEA-F-SPIDER based pulse characterization setup suitable for IR pulses with over octave spanning spectra, compared it to SHG-FROG measurements and pointed out challenges of pulse measurement techniques for sub-cycle pulses in the IR range. In addition, X-SEA-F-SPIDER provides spatio-temporal information which can be useful to judge the pulse fidelity across the beam. Potentially, it allows single-shot pulse measurements, thus completely avoiding coherent artefact issues related to multi-shot techniques [39]. The prospects of characterization of even longer wavelength pulses in the mid-IR spectral range are explored, and the described technique provides tools vital for the development of sources in this difficult spectral range.

Acknowledgments

We acknowledge funding by the Austrian Science Fund (FWF): P 27577-N27 and SFB NextLite F4903-N23.

#261180 Received 15 Mar 2016; revised 25 Apr 2016; accepted 25 Apr 2016; published 1 Jun 2016